

PRELIMINARY ASSESSMENT OF TERMOSKAN OBSERVATIONS OF MARS

B. MURRAY¹, M.K. NARAEVA², A.S. SELIVANOV², B.H. BETTS¹, T. SVITEK¹,
V.D. KHARLAMOV², A.V. ROMANOV², M.L. SANTEE¹, Y.M. GEK TIN²,
D.A. FOMIN², D.A. PAIGE³, A.S. PANFILOV², D. CRISP^{1,4},
J.W. HEAD⁵, S.L. MURCHIE⁵, and T.Z. MARTIN⁴

1. California Institute of Technology, Pasadena, California, USA
2. Institute for Space Devices, Moscow, USSR
3. University of California, Los Angeles, California, USA
4. Jet Propulsion Laboratory, Pasadena, California, USA
5. Brown University, Providence, Rhode Island, USA

(Camera-ready copy received 18 September 1990)

(Contribution Number 4820 of the Division of Geological Sciences of the
California Institute of Technology)

Abstract. In February and March, 1989, the Termoskan instrument onboard the Phobos '88 spacecraft acquired a limited set of very high resolution observations of the 8–12 μm thermal emission from Mars' equatorial regions. Simultaneous and coincident observations were acquired in the 0.5 to 1.0 μm region also. We have evaluated quantitatively about 25% of those data and find close agreement with the lower-resolution Viking Orbiter Infrared Thermal Mapper (IRTM) observations, demonstrating the accuracy of the Termoskan system. Termoskan's thermal emission panoramas display limb brightening at the morning limb, which we interpret as arising from the presence of a diurnal ice crystal haze there. Detached hazes at high altitude also are evident in the visible panorama of the evening limb. The Phobos '88 orbit enabled Termoskan to record the visible shadow from the Martian moonlet Phobos and to measure the surface thermal response to that shadow's passage. Analysis of one such data set shows that the uppermost fraction of a millimeter is two to four times more insulating than the uppermost centimeters sensed by the IRTM experiment. The Termoskan data are of direct importance to the planning and execution of the PMIRR and TES experiments of the U.S. Mars Observer mission to be launched in 1992. An improved version of Termoskan is planned for the Mars '94 mission of the U.S.S.R. Those data will be of still higher surface resolution and, thus, complement well the expected PMIRR and TES global data sets.

1. INTRODUCTION

On February 11, March 1, and March 26, 1989, the Termoskan instrument onboard the Phobos '88 spacecraft of the USSR measured the reflected solar and emitted thermal radiation from Mars' equatorial region at very high spatial resolution. A complete mapping covering $\pm 52^\circ$ of latitude was originally planned, but the premature failure of the Phobos '88 spacecraft frustrated that goal. However, the existing Termoskan data have proven to be of very high quality and enable new scientific conclusions about Mars.

The instrument team of the Glavcosmos organization in the U.S.S.R. published the first results of the experiment in Selivanov, *et al.*, (1989). Subsequently, a combined Soviet and US scientific team made a preliminary quantitative evaluation of about 25% of the entire data set. The present paper communicates our findings. We find close agreement with the Viking IRTM (Infrared Thermal Mapper) brightness temperatures, confirming the accuracy of the Termoskan system and calibration. We recognize a novel pattern of emission from particles, probably water ice, suspended in the morning Martian atmosphere. Ther-

mal emission from surface features is varied and distinct down to the limit of resolution. Finally, we have detected the presence of unusually insulating material in the uppermost fraction of a millimeter of the Martian surface in places where the shadow of the Martian moon Phobos briefly eclipsed the surface.

II. THE EXPERIMENT

Termoskan is a two-channel optical-mechanical scanning radiometer. Figure 1 shows its optical layout. Radiation flux is sent by the scanning mirror (1) to the parabolic mirror (2) and then after filtering (3) and (4) to the detector (5) in the range 8.5–12 μm and to the detector (7) in the range 0.6–0.95 μm . To ensure radiometric measurements there are calibration units (10) and (12). Calibration with them and with open space (11) is carried out for each line of the information transmitted. The displacement of the instantaneous field of view by the scanning mirror provides line scanning in the direction perpendicular to the spacecraft motion vector. Frame scanning results from the orbital motion of the spacecraft itself. The instrument was fixed to the spacecraft, pointing in the anti-solar direction. There was no scan platform. The instantaneous field of view was 0.9 angular minutes, the scanning angle was 6.1°, the scanning frequency was 1 line per sec., and the swath width was 384 pixels. This arrangement allowed a resolution at nadir of 1.8 \times 1.8 km from an altitude of 6300 km with a swath width of 650 km. The duration of the survey session determined the length of the panoramic view. Figure 2 shows the Termoskan spectral response, and Table 1 summarizes the optical and signal characteristics. Figure 3 shows the calibration of the thermal channel.

TABLE 1. Termoskan Instrument and Signal Parameters

Weight	28 kg
Aperture	150 mm
Focal length	375 mm
Scan rate	1 line/second
Instantaneous Field of View	0.26 mrad per pixel
Infrared detector	HgCdTe
Visible Detector	Photodiode Si
Spectral Bands: Visible	0.5–0.95 microns
Infrared	8.5 – 12.0 microns
Data pixels per line	384
Calibration: Visible	Onboard lamp
Infrared	Onboard black body and space
Bits per pixel	8
Temperature sensitivity (K)	0.5 at 240 K
Temperature range (K)	170–290

There is noise equivalent to approximately 1–2 degrees Kelvin in every 8th sample of the infrared images.

Four Termoskan observing sessions were carried out. Each provided a thermal emission and a visible panoramic view of the surface. Most of the equatorial area was surveyed (Table 2 and Figure 4). The survey was done in the mode of continuous sun - star orientation of the Phobos spacecraft. The optical axis of the Termoskan instrument closely coincided with the direction of the Sun's rays. In the February 11 session, when minimum distance was only 1150 km, the thermal emission and reflected light profiles exhibited longitudinal gaps of varying size between scan lines. Each scan in the North - South direction, however, maintained full resolution and coverage. In the remaining sessions the survey altitude was 6300 km. In this case, line and frame scanning correspond; therefore geometrical distortions occur only because of the sphericity of the planet. Each session on the 26th of March lasted one hour. This interval was sufficient for Termoskan to cover the Martian surface from limb to limb. In these sessions Termoskan imaged the shadow of Phobos on the surface of Mars.

III. THE TERMOSKAN PANORAMAS

The digital Termoskan data received from the Phobos 2 spacecraft were converted into high quality photographic displays. Portions of the first of the March 26 panoramas are reproduced in condensed form in Figures 5 and 6. Selivanov, *et al.*, (*Nature*, 1989) present a preliminary discussion of the February 11 and March 1 panoramas. Here we consider the March 26 data set qualitatively and we include some digital analysis of key attributes of all the photographic renditions. February 11, March 1, and March 26, 1989 correspond to areocentric solar longitude (L_s) values of 356, 6, and 18, respectively, which is northern spring on Mars. The panoramas encompass a significant portion of the equatorial regions of Mars. The Tharsis volcanic ridge, Vallis Marineris, and anomalously low thermal inertia areas like Memnonia which were first recognized in the Viking IRTM data and subsequent analyses (Kieffer *et al.*, 1977; Palluconi and Kieffer, 1981) are all included.

A conspicuous attribute of the Termoskan panoramas is the much lower contrast in the photographic displays of the visible channel versus the thermal infrared. Indeed, this difference is even more striking when viewed in the unstretched digital data, for example in Figure 11. A factor contributing to the low visible contrast is the zero phase angle observations of the Termoskan measurements. Shadows on the Martian surface arising from large-scale relief and from topographic slopes were not visible. Careful analysis of the limb profiles, and of Phobos shadow images discussed in later sections, shows that instrumental scattering in the Termoskan optics was negligible.

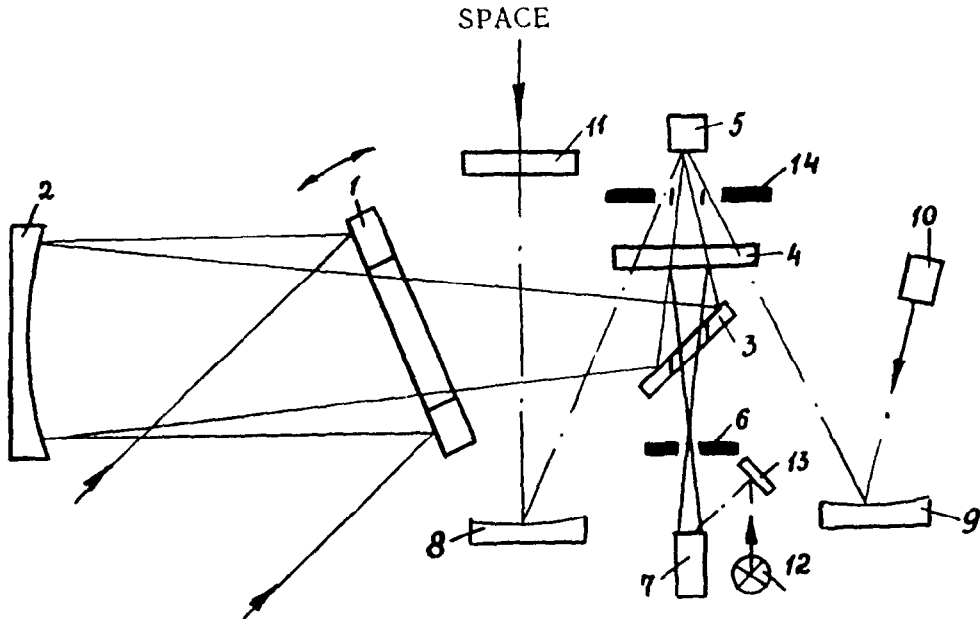


Figure 1: Optical block diagram of the Termoskan instrument. 1 – Scanning mirror; 2 – parabolic mirror; 3 – mirror with hole in center; 4 – IR-filter; reflects visible light and transmits IR; 5 – photosensor of the IR-channel; 6 – diaphragm of the visible channel; 7 – photosensor of the visible channel; 8, 9 – spherical mirrors used for calibration; 10 – “hot” radiator (IR blackbody calibrator); 11 – protective glass of the space calibration channel; 12 – calibration lamp; 13 – mirror; 14 – modulator.

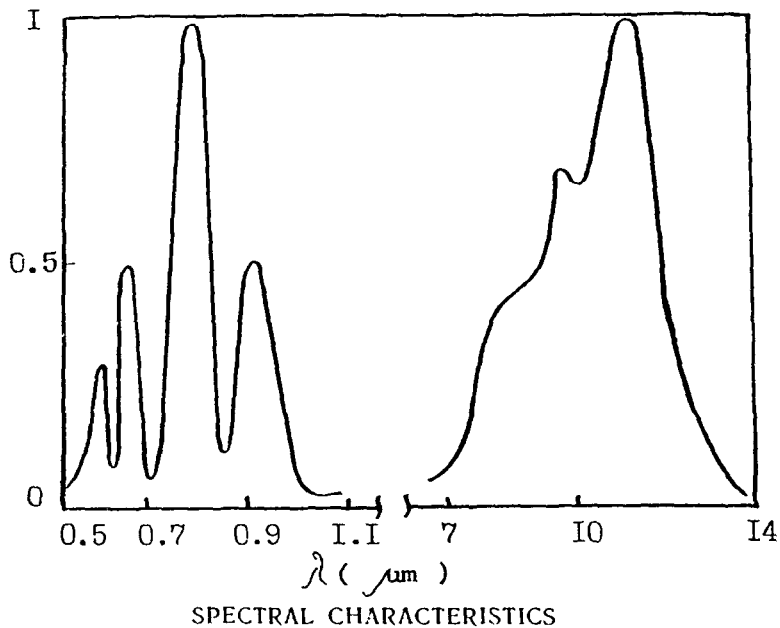


Figure 2: Spectral response of the Termoskan solar and infrared channels.

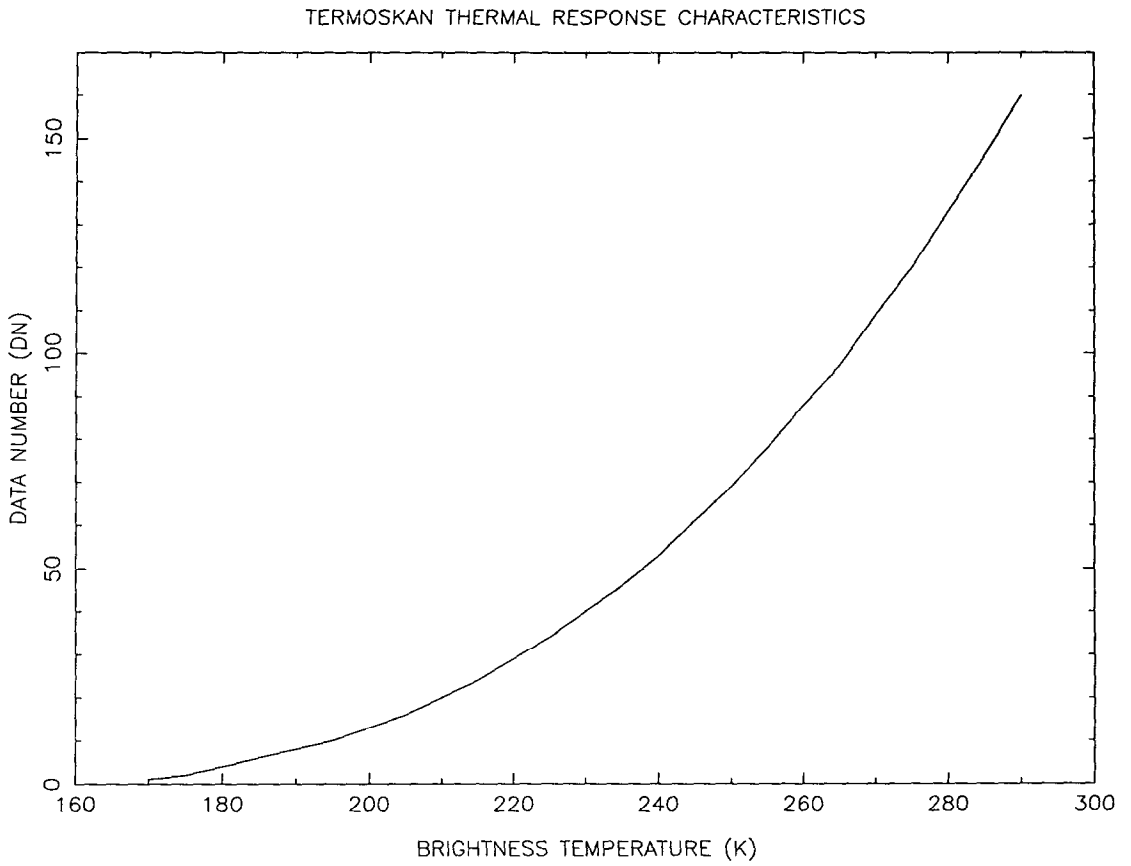


Figure 3: Termoskan infrared calibration curve.

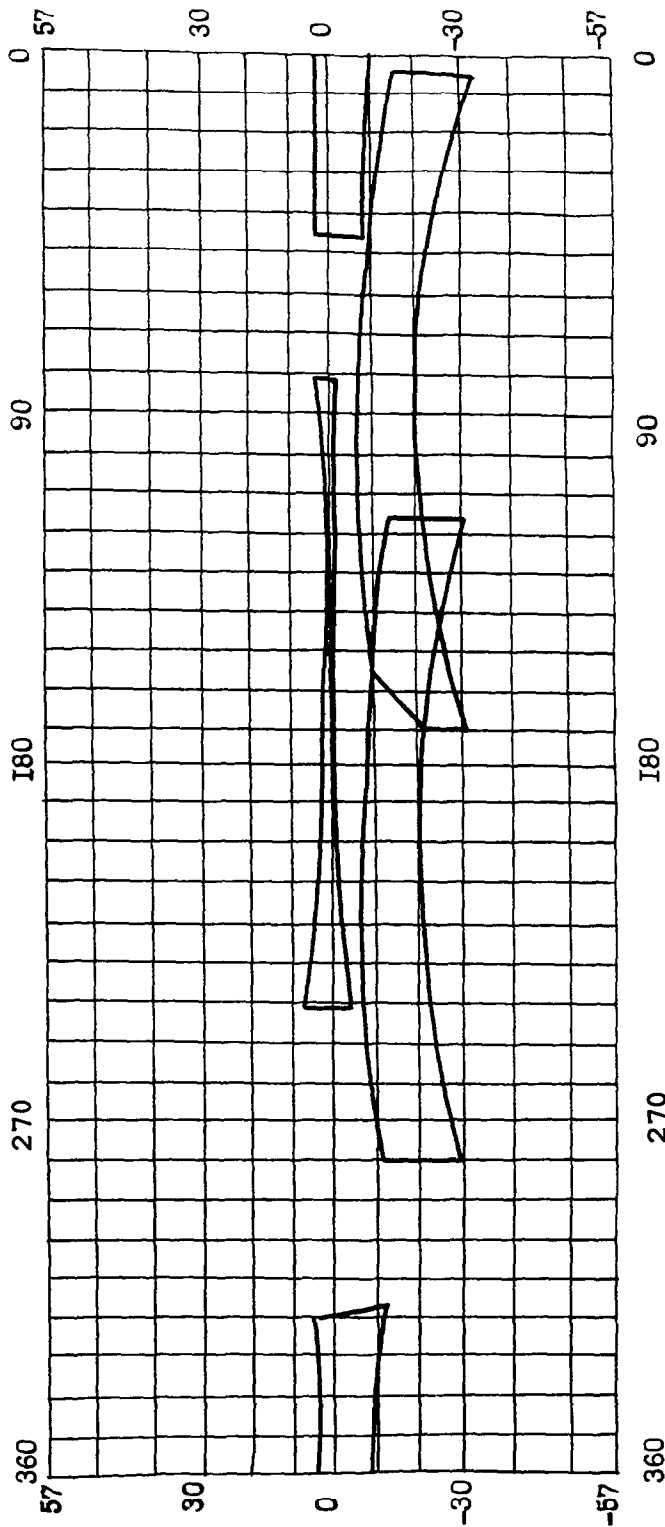


Figure 4: Coverage of the surface of Mars by the four Termoskan panoramas.

TABLE 2: SUMMARY OF TERMOSKAN DATA SET

Date	Start Time (UT)	Stop Time (UT)	Longitude	Latitude	Local Time of Day	Minimum Altitude (km)	Resolution per pixel (km)	Total Number of Lines	Morning Limb in scan	Evening Limb in scan	Phobos Shadow in scan
1A	2-11-89 10 55 00	11 26 04	357 80-240	6N-4S	6.0-18.0	1150	.3	1864	No	No	No
1B	2-11-89 10 55 00	11 26 04	357 80-240	6N-4S	6.0-18.0	1150	.3	1864	Yes	No	No
2A	3-01-89 13 12 00	13 52 00	6 317-0-49	5N-12S	9.6-16.5	6300	1.8	2400	No	No	No
2B	3-01-89 13 12 00	13 34 50	6 4-49	5N-8S	9.6-13.0	6300	1.8	1370	No	No	No
3A	3-26-89 09 11 29	10 11 29	18 5-170	7S-30S	6.3-17.6	6300	1.8	3600	Yes	Yes	Yes
3B	3-26-89 09 11 29	10 11 29	18 5-170	7S-30S	6.3-17.6	6300	1.8	3600	Yes	Yes	Yes
4A	3-26-89 16 48 30	17 49 50	18 115-280	7S-30S	6.3-17.6	6300	1.8	3680	No	No	Yes
4B	3-26-89 16 48 30	17 23 30	18 185-280	7S-30S	6.3-17.6	6300	1.8	2100	Yes	No	Yes

Termoskan acquired a total of 4 strips across Mars. In the above chart, A designates infrared data, and B designates visible data; e.g., scans 1A and 1B were acquired simultaneously with 1A consisting of infrared data and 1B consisting of data from the visible channel.

Start and stop times given are times at the spacecraft, not ground receive times.

All scans were acquired in 3 axis, sun-star stabilized mode. There was no scan platform. Termoskan looked along the Sun-spacecraft line (i.e. zero phase angle), except for slight rocking motions of the spacecraft.

Because Scan 1 was acquired near the periapse of one of the early elliptical orbits, the scan is very undersampled.

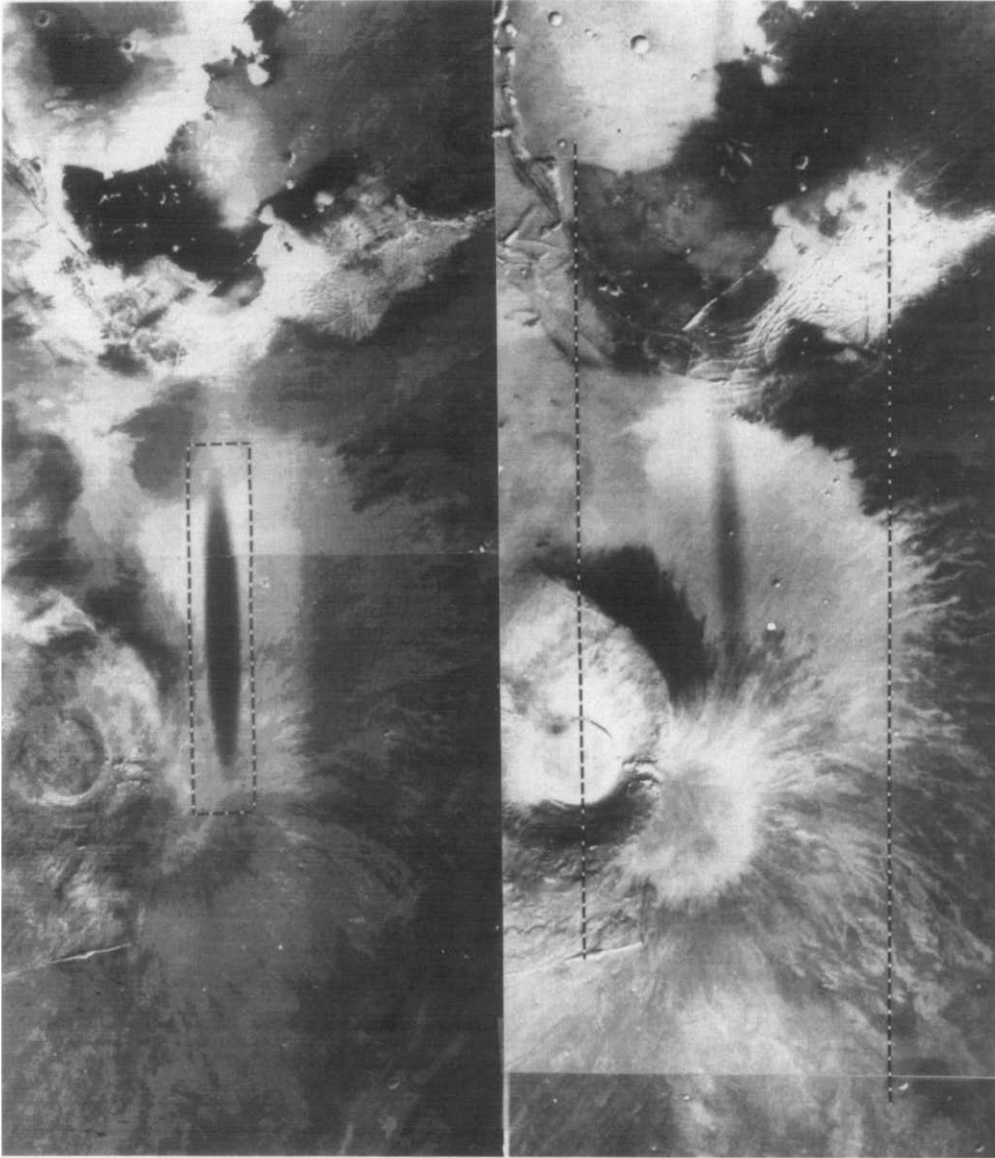


Figure 5: Visible (top) and infrared (bottom) data from the first of the March 26 panoramas. North is toward the top. The Phobos shadow used for analysis can be seen within the boxed portion of the visible data. The two lines in the IR data represent the center lines of the strips of data which are compared with IR data in Figures 8 and 9. Warmer areas appear bright in the IR image.

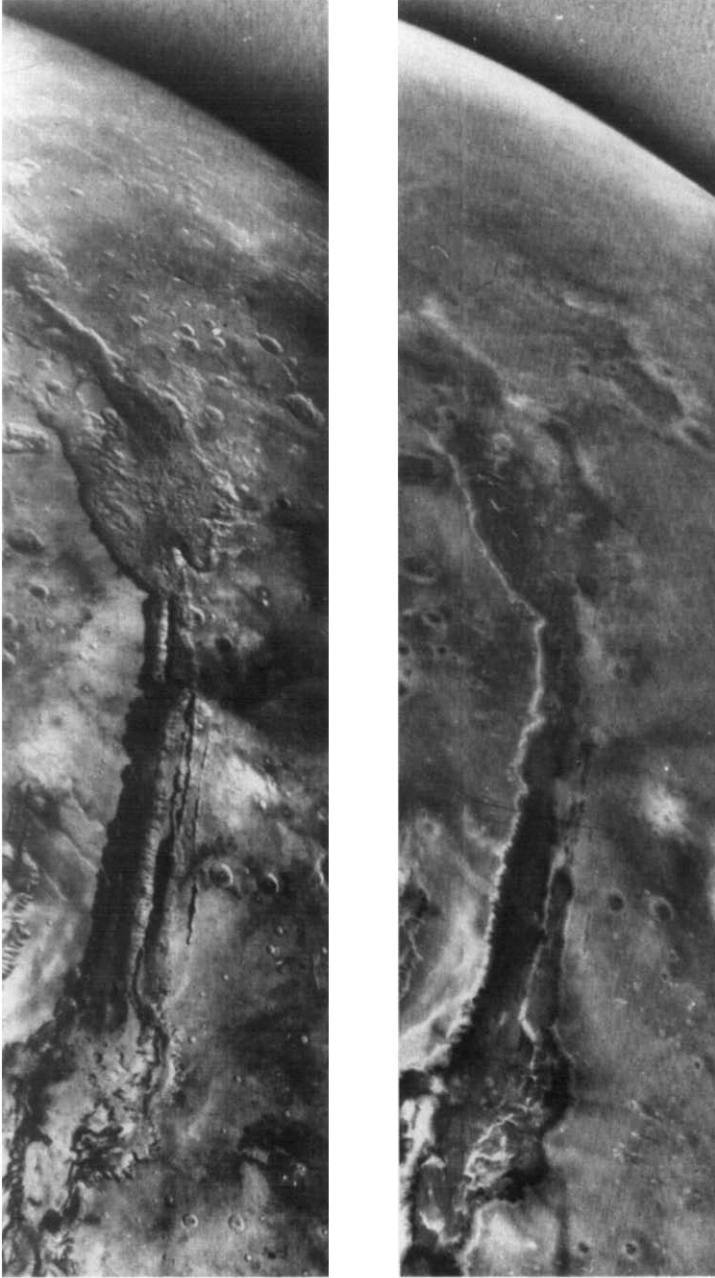


Figure 6: Visible (bottom) and infrared (top) data from the first of the March 26 panoramas. North is toward the top. The eastern end of Valles Marineris appears in the center of the images. The evening limb can be seen at the right.

Rocket propulsion products and induced vibrations always pose the threat of fine dust contamination of space optics. Thus an inflight demonstration of the absence of instrumental scattering is very desirable. Analysis of Viking Data has shown that atmospheric dust and other aerosols will cause a lack of surface contrast at visible wavelengths (Thorpe, 1979). We therefore conclude that scattering by dust and ice crystals in the Martian atmosphere is responsible for the very low surface contrast in the visible channel. The difference in contrast between the visible and infrared channels implies that the visible wavelength optical depth is significantly larger than the thermal infrared optical depth. This result is consistent with the results of Toon, *et al.*, 1977, Pollack, *et al.*, 1979, Martin, *et al.*, 1979, and Zurek, 1982 whose work on Mariner 9 and Viking data implies for this season visible to infrared optical depth ratios of order 2 or greater. Derivation of numerical optical depths from Termoskan data and comparison with previous studies will be an interesting subject of our future work.

Fortunately for scientific studies of the Mars surface, the thermal emission channel yielded very high contrast data. This attribute is clear not just in the photographic renditions but in the actual digital data as, for example, in Figures 11 and 12. This circumstance reflects in part the excellent qualities of the instrument itself. The Modulation Transfer Function of the entire Termoskan system must have been very high in order for abrupt pixel-to-pixel variations in signal to be recognized. In addition, the bulk of Mars' atmospheric scattering at visible wavelengths probably arises from particles in the half to 2.5 micron range (Pollack, *et al.*, 1979). These are too small and too cold to be discernable emitters in the 8 to 13 micron region (except at the limb). Furthermore, the dominantly high-sun observational conditions of the displayed Termoskan images enhance the visibility of thermal differences arising from albedo, texture, and slope variations. Modelling studies predict variations of tens of Kelvins.

Ultimately, it will be possible to quantify the causes of Termoskan thermal variations across the surface, especially using the high resolution thermal inertias derived from the Viking IRTM data set by Christensen and Malin (to be published). The thermal model of Clifford *et al.*, is suitable and available for interpreting the new Termoskan data. We expect that the Termoskan data will yield important new geologic information.

IV. COMPARISON WITH VIKING IRTM OBSERVATIONS

A critical first step was to determine the absolute accuracy of the Termoskan data set. We compared brightness temperatures from Termoskan's infrared

channel to brightness temperatures from IRTM's 11 micron channel (9.8 to 12.5 microns). We constrained the IRTM data to match approximately the Termoskan data in season (L_s), longitude, latitude and local time of day. In selecting our constraints we had to balance matching those parameters accurately with obtaining a statistically significant number of IRTM points to compare with those Termoskan scans for which digital data was available in the U.S. Of the regions analyzed so far, the largest number of suitable IRTM points corresponds with a section of Termoskan panorama 3. Figure 7 shows the latitudes and longitudes of IRTM points that match this section of panorama 3 to within ± 10 degrees of L_s and ± 30 minutes of local time. Using these IRTM data, we show in Figure 8 a comparison of IRTM and Termoskan data for a strip of constant latitude which is two degrees wide and centered upon -18 degrees latitude. In order to compare the two data sets, we degraded the Termoskan resolution to a resolution comparable to Viking. Thus, in Figure 8 the dark line represents Termoskan data that have been averaged in 67×67 pixel squares (approximately 2 degrees by 2 degrees). The lighter line is a one pixel Termoskan strip for reference. The IRTM data are represented by dots with horizontal error bars. These "error bars" represent the size of the footprint of each IRTM data point. Local time of day in these data ranges from about 8.5 to 10.3 hours.

After comparing each IRTM point with the averaged Termoskan point of the same longitude, the average temperature difference between Termoskan and IRTM is 3.1 ± 0.4 K with the Termoskan temperatures being warmer. Note also in Figure 8 that qualitative features match well between the two data sets. Figure 9 shows an analogous graph centered upon -9.5 degrees latitude. For these data the average temperature difference is 3.2 ± 0.5 K, a result consistent with that obtained from the data in Figure 8 and from other latitudinal strips that we have examined. Ignoring possible errors in the decalibrated Viking IRTM data, this 3K difference includes any bias in the Termoskan absolute preflight calibration. Also included is any intrinsic difference in Mars' thermal emission between 1976-78 and 1989, including atmospheric effects such as clouds. Furthermore, the 3K difference also includes the effects of the somewhat different bandpasses of the Termoskan IR channel and the Viking 11 mm channel (Kieffer, *et al.*, 1977). The peak of the Termoskan response actually falls between that of the Viking's 9 mm and 11 μ m channels. We compared Termoskan with sparsely available Viking's 9 mm data as well. The IRTM 9 μ m data that are available for the region studied average about 1.5 K higher than those of the IRTM 11 μ m channel. Thus, the average temperature difference between Termoskan and the IRTM for 9 μ m channel seems closer 1 to 2 K. We conclude that for the region analyzed, the Termoskan IR data may differ

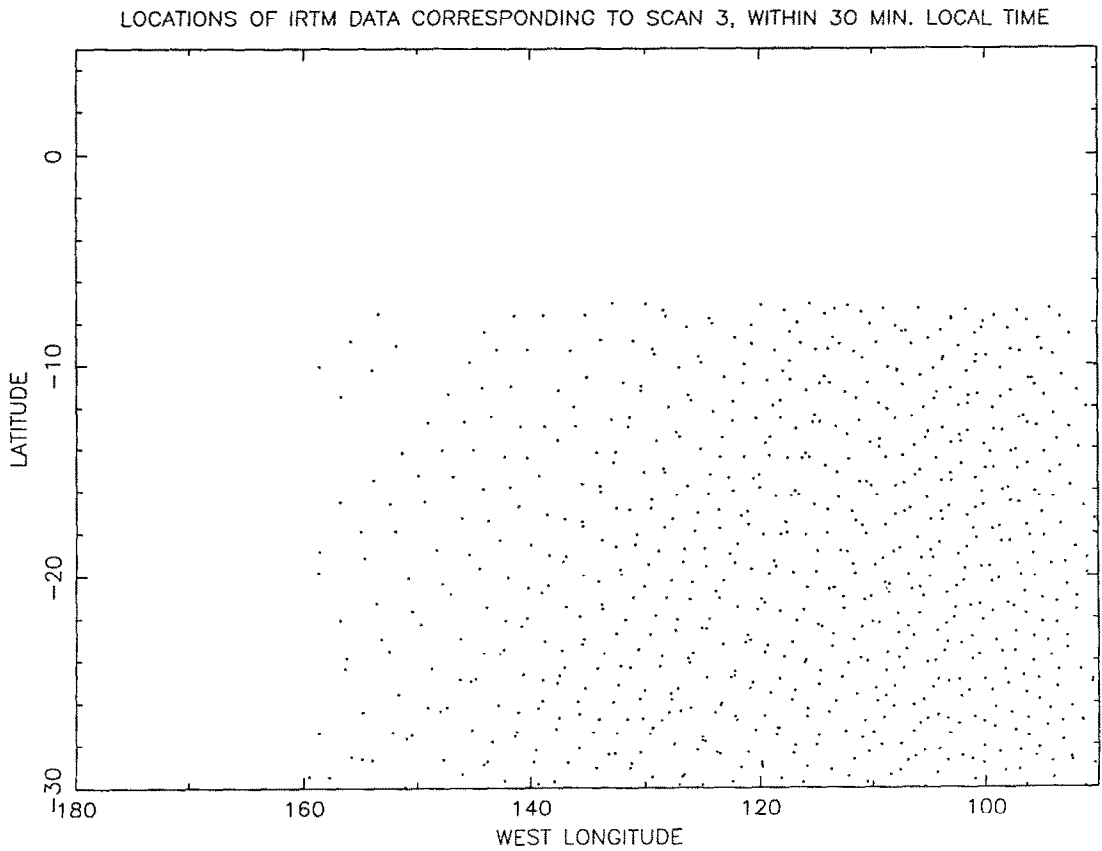


Figure 7: Plotted are the locations of the IRTM points which match this section of panorama 3 to within ± 10 degrees of L_s and ± 30 minutes of local time.

σ : $-18^{\circ}0 \pm 1^{\circ}0$ LAT.; TERMO. DATA: 67 PIXELS SQUARE AVG.; ± 30 MIN.

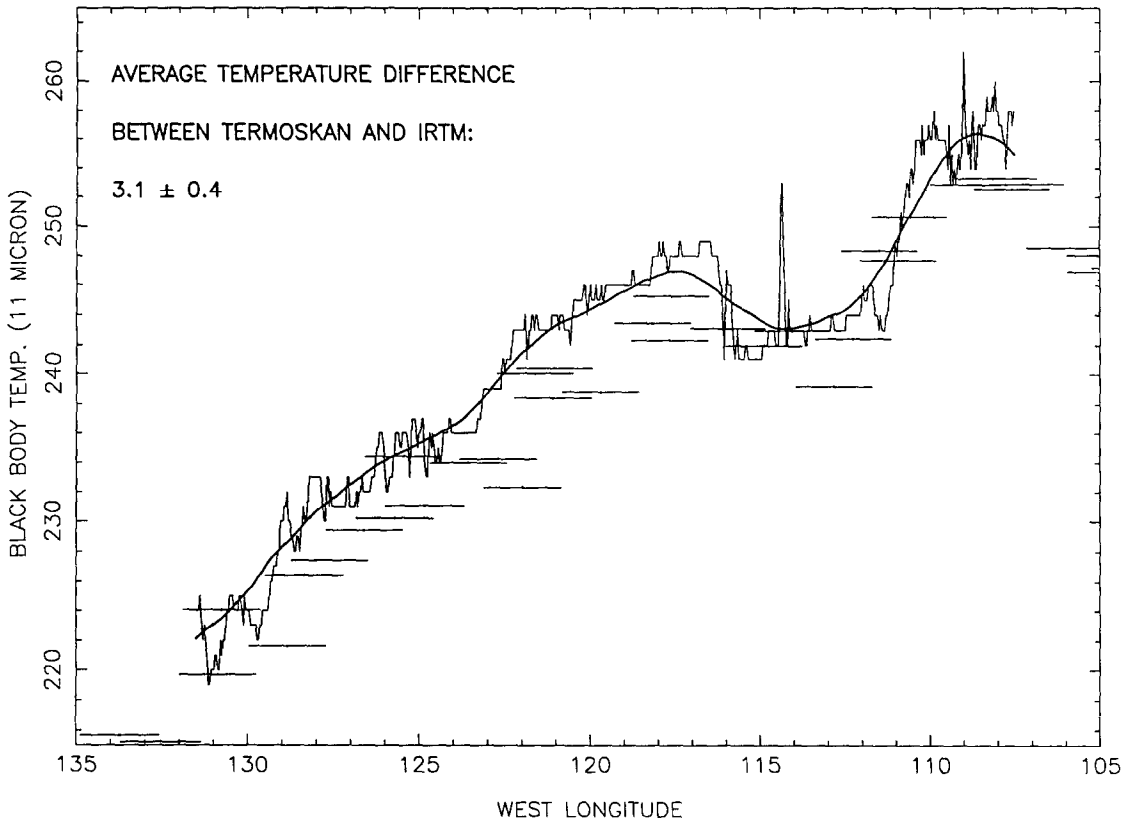


Figure 8: Comparison of Termoskan data with analogous IRTM data for a 2 degree wide strip of constant latitude centered on -18 degrees. The dark line represents a sliding boxcar average of Termoskan data which has been averaged in 2×2 degree squares. The lighter line is a 1 pixel Termoskan strip for reference. The points represent IRTM data with the error bars representing the footprint of each IRTM data point. IRTM data is constrained to match the Termoskan data to within ± 10 degrees of L_s and to within ± 30 minutes of local time. After comparing each IRTM point with the averaged Termoskan point of the same longitude, the average temperature difference between Termoskan and IRTM is 3.1 ± 0.4 K with the Termoskan temperatures being warmer. Local time of day in the data shown ranges from about 8.5 to 10.3. The lower line in the infrared image shown in Fig. 5 corresponds to the center of the comparison strip.

σ : $-9^{\circ}5 \pm 1^{\circ}0$ LAT.; TERMO. DATA IS 67 PIXELS SQUARE AVG.; ± 30 MIN.

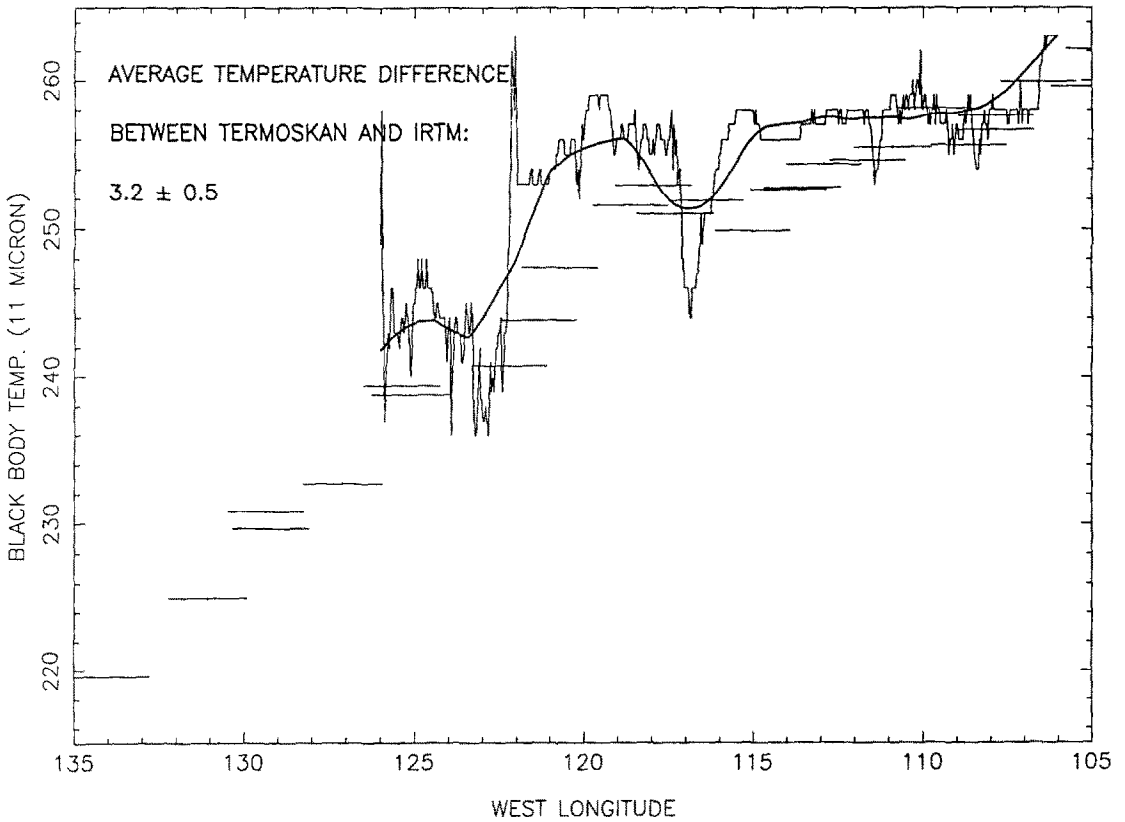


Figure 9: Analogous plot to Figure 8 for -9.5 degrees latitude. The upper line in the infrared image shown in Figure 5 corresponds to the center of the comparison strip.

σ : $-18^{\circ}0 \pm 1^{\circ}0$ LAT.; PIXELS WIDE=1,11,67; ± 30 MIN. TOD

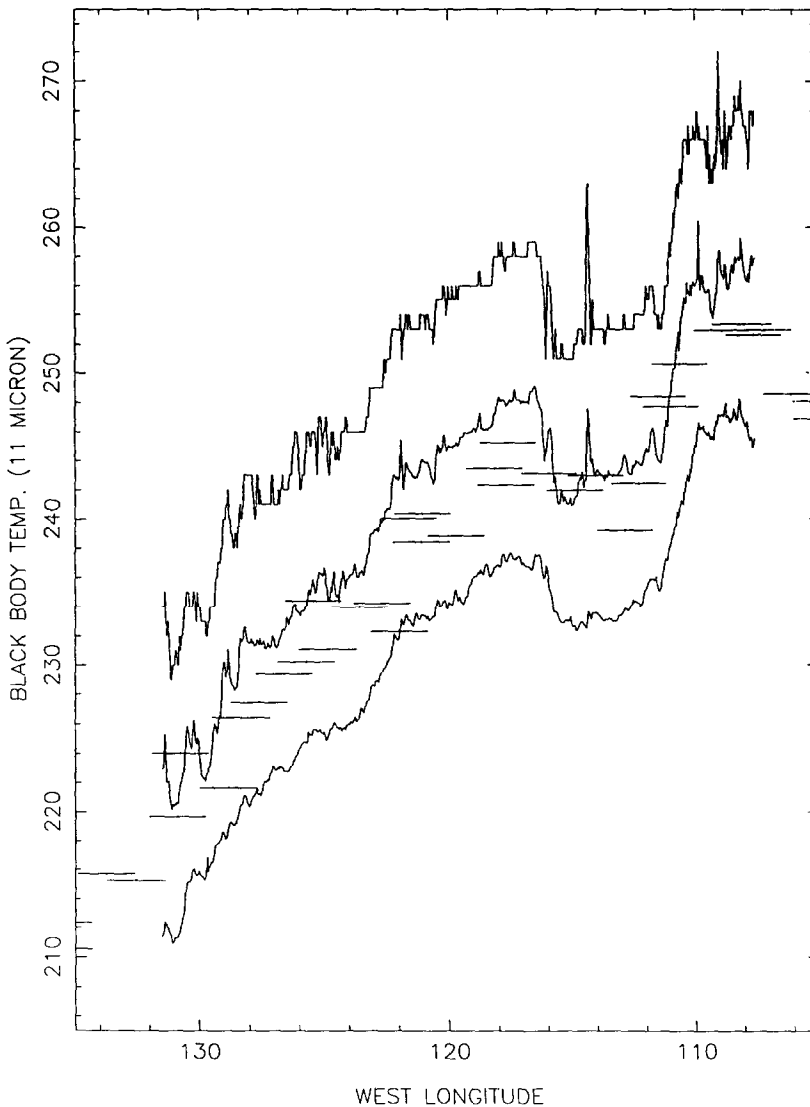


Figure 10: The lines represent Termoskan data centered upon -18 degrees latitude. Curve 1 (top) has no averaging, it is a 1 pixel wide strip to which 10 K have been added uniformly to ease comparison with the other curves. Curve 2 (middle) has 11 pixels averaged in a North-South direction. Curve 3 (bottom) has 67 pixels averaged in a North-South direction, and has had 10 K subtracted from it. Note that sharp features can be seen in the 1 pixel wide strip that average out at lower resolutions, e.g. the spike at approximately 115 W. corresponds to the rim of a 6 km diameter crater.

by no more than 2 K from comparable IRTM data. The thermal features in Termoskan correlate very well with the lower resolution IRTM. Termoskan sees thermal variations even at the limit of its spatial resolution.

Figure 10 again shows Termoskan and IRTM data for -18 degrees latitude. The three curves represent different degrees of spacial averaging of the Termoskan data. Curve 1 is not averaged, i.e., it is a 1 pixel wide strip; curve 2 has 11 pixels averaged in a North-South direction; and curve 3 has 67 pixels averaged in a North-South direction. None of the curves are averaged in an E-W direction (whereas, Figures 8 and 9 were). Thermal features remain at the limit of resolution of the 1 pixel curve. For example notice the spike at approximately 115 W. Longitude (in Fig. 10). This corresponds to the sunlit rim of a 6 km diameter crater.

V. TERMOSKAN LIMB PROFILES

Three of the four visible and thermal panoramas include the morning limb, and one includes the evening limb as well. The limb profiles of March 26 have a vertical resolution of approximately 3 km/pixel, which approaches that of the Viking Orbiter Camera (Jaqin *et al.* 1986). The limb profiles from the February 11 panorama have a vertical resolution of about 1.3 km/pixel in the NS direction and are somewhat coarser in the EW direction. These data offer the promise of an important increment in understanding the vertical structure of Mars' atmosphere. They have significance for the execution and analysis of the limb-sounding experiment of the Mars Observer Pressure Modulator Infrared Radiometer instrument (PMIRR) on Mars Observer. Specifically, we report here the discovery of limb brightening in the thermal emission from the morning limb, and offer an explanation.

Figure 11 shows a single morning limb profile from panorama 3 in both the visible (dashed curve) and infrared (solid curve) channels. The data numbers for each channel are plotted as a function of the elapsed time (sec.) from the beginning of the scan. The instrument moved from an arbitrary point off the morning limb, across the limb, and onto the surface of Mars. Offsets in pixel number in both the direction of scanning and along the length of the frame exist between the files containing the infrared and the visible data. These offsets are artifacts introduced when the data were extracted from the primary record. By matching surface features that are clearly recognizable in both the visible and thermal emission images, we have repositioned the visible and infrared profiles within a relative accuracy of 1-3 pixels for the specific profiles shown in this paper. Figure 12 shows a second morning limb profile also taken during scan 3.

The absolute time of limb crossing is not available accurately enough solely from trajectory information to

identify the pixel corresponding to the limb position. That would require 1-3 km absolute orbital knowledge. Furthermore, the spacecraft rocked slightly about the anti-solar direction in response to its attitude control system (see Figure 15). These slow deviations (which were not monitored during the data-taking session) introduce only an insignificant distortion into the panoramas. Yet, the absolute time the limb crossed the Termoskan field of view may be uncertain by 10 or 20 seconds due to this slow deviation from the precise anti-solar direction. (Analogous problems in determining the absolute location of Phobos' shadow are discussed later). We expect eventually to recover the limb position accurately and confidently by fitting the planetocentric coordinates of identifiable surface features to the known dimensions and orientation of Mars. From our preliminary analysis here, we believe the limb was encountered near the point where the infrared signal was first detected. The preliminary Soviet spacecraft data places the limb crossing at about 26 seconds — close to the beginning of the infrared signal.

The effect of limb brightening in the thermal emission is evident in both morning limb scans, Figures 11 and 12. It is evident in the higher resolution data from February 11. Limb brightening in thermal emission usually arises from viewing a partially transparent atmosphere containing a temperature inversion. It is difficult to imagine a plausible purely surface origin, though in theory it might be possible. An atmospheric effect is our preferred explanation, particularly since we see the limb brightening over a very large range of latitudes. In the present case, a discernable peak in thermal brightness just off the limb means the dawn atmosphere was warmer than the surface. Furthermore, the atmosphere must have contained a sufficient abundance of thermally emitting particles (dust or ice) to supply the needed flux. Mars' atmospheric gasses are nearly transparent at Termoskan's spectral passband. Mariner 9, Viking Orbiter, and Viking Lander observations together suggest that this requirement could be satisfied near the morning terminator. A diurnal predawn ice-crystal fog often forms (Jakosky, 1985). (Still, some abundance of dust particles is always to be expected in the Mars atmosphere).

The high emissivity of Mars' surface allows it to cool more efficiently during the night than can the gas-dominated atmosphere. An early-morning atmospheric temperature inversion results. We infer that the sharp peak in thermal emission corresponds to the maximum atmospheric path length sensed just before limb crossing. Once the limb was crossed, Termoskan sensed a decreasing fraction of emission from the warmer atmosphere and an increasing fraction from the colder surface. The composite signal began to decline in magnitude from the peak, or remained constant (as in Figure 12). As the scan continued, the emission angle to surface decreased. The instrument

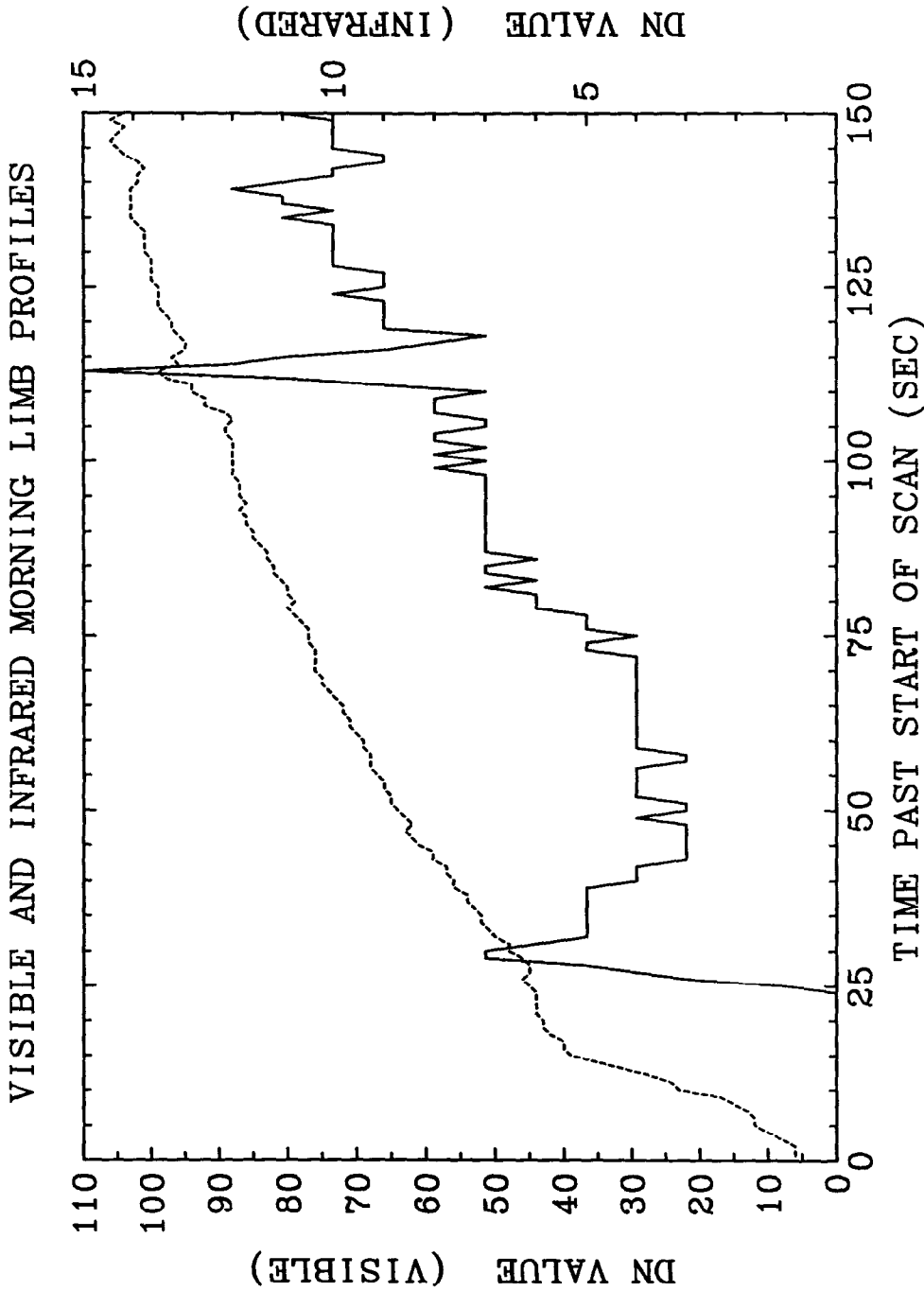


Figure 11: A single morning limb profile for both the visible (dashed curve) and the infrared (solid curve) channels. The solid limb was encountered at approximately 26 seconds after the start of the scan. Note the IR limb brightening seen at 26 seconds and the crater rim seen at 113 seconds.

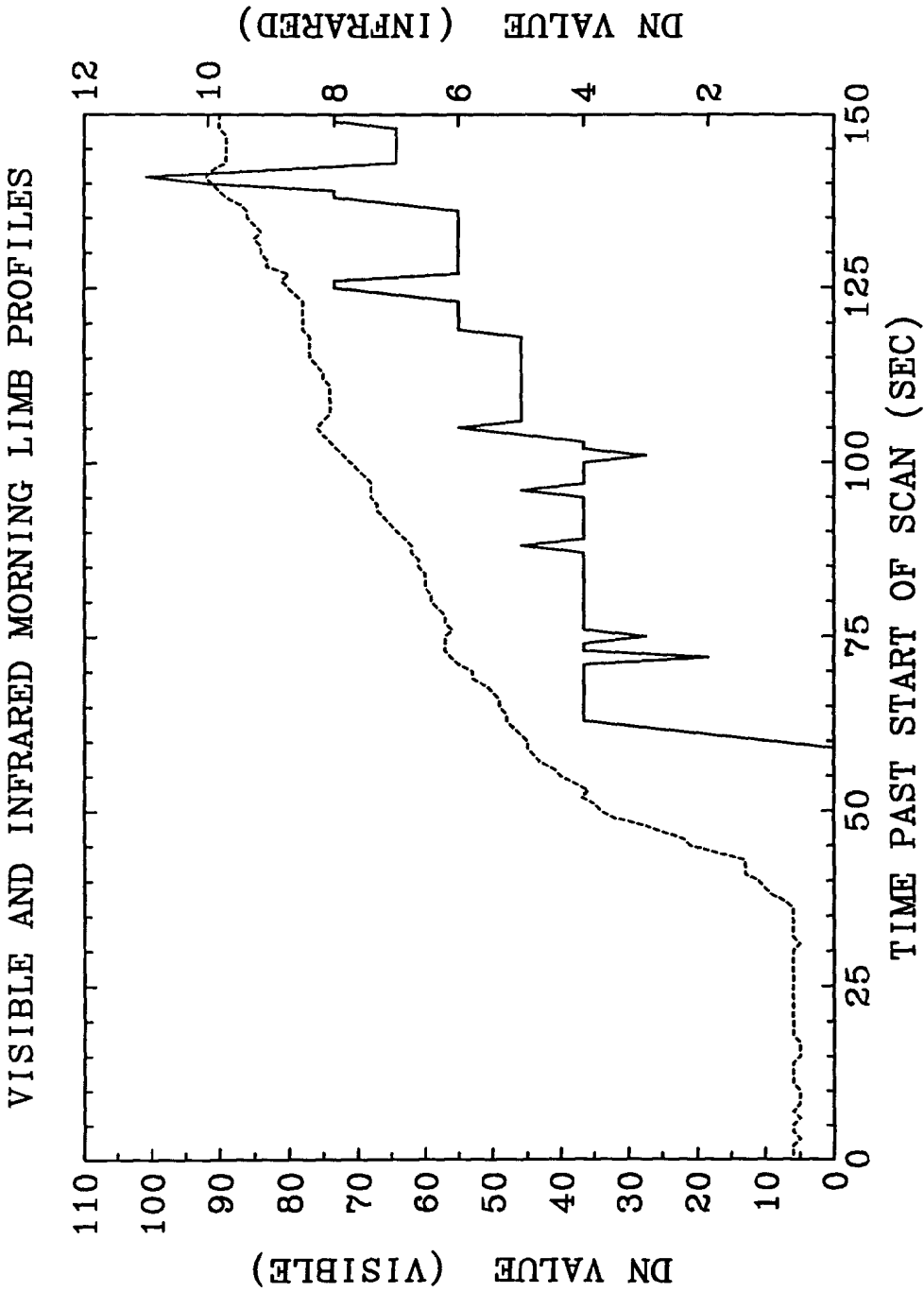


Figure 12: Another 1 pixel wide morning limb profile for both the visible (dashed curve) and the infrared (solid curve) channels. Note that in this IR profile, the signal levels off rather than dropping from the limb brightened peak.

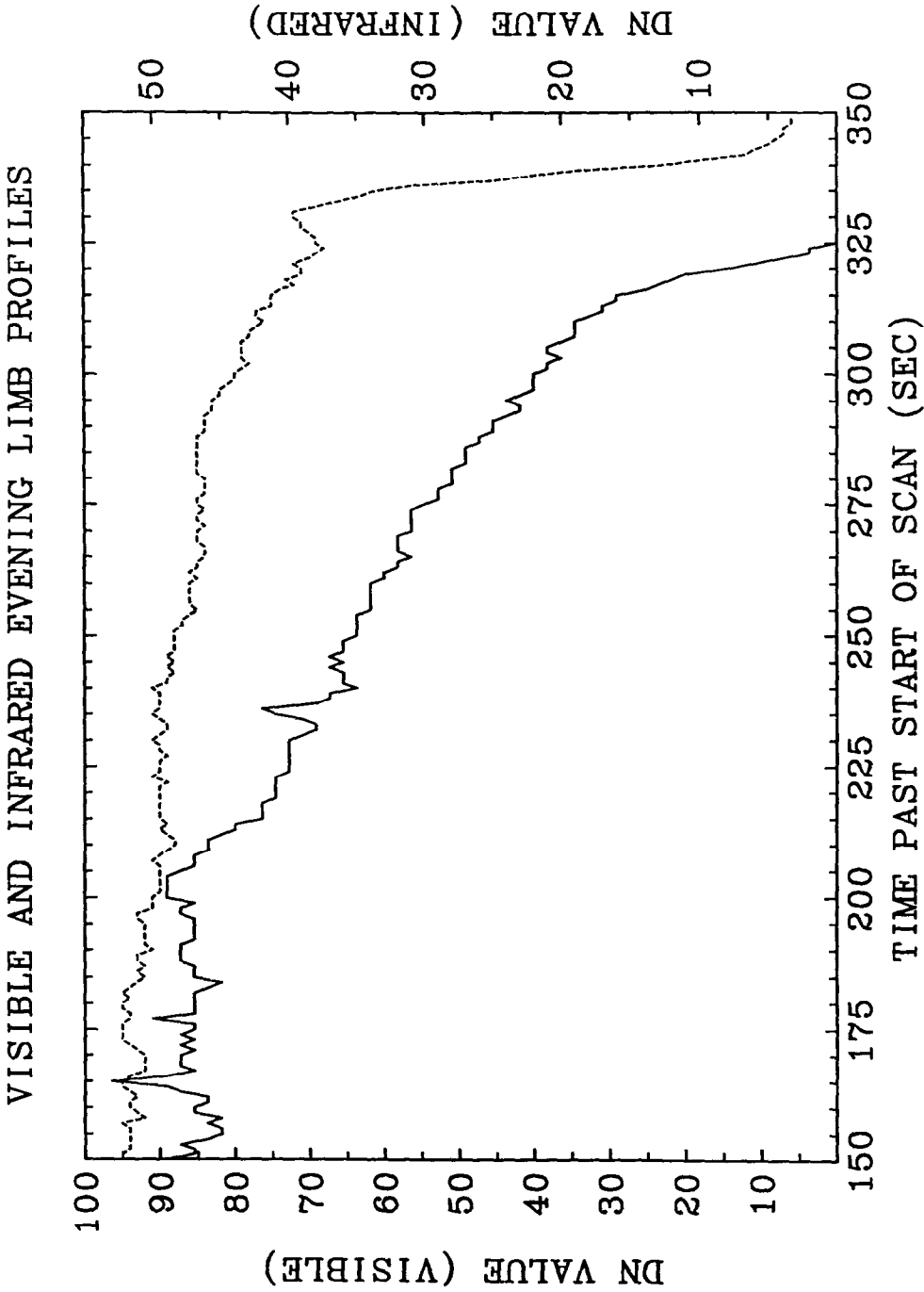


Figure 13: A single evening limb profile for both the visible (dashed curve) and the infrared (solid curve) channels. Note that the times on the horizontal axis are local to the particular data file and do not represent actual times along the scan. Notice that there is no IR evening limb brightening.

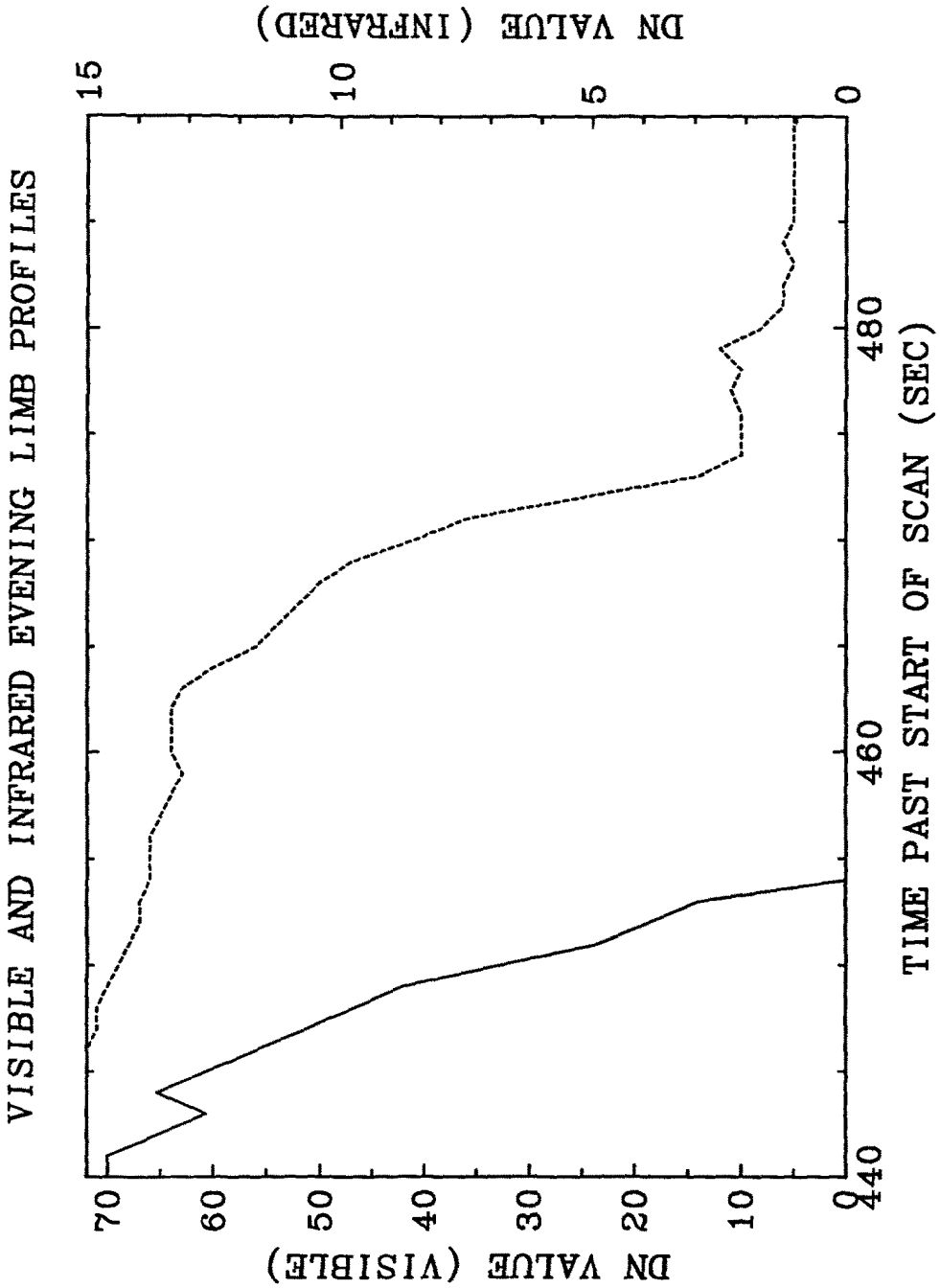


Figure 14: Another single evening limb profile seen this time on a different scale. Again times are local to the particular data file. Note the peak in visible brightness at 479 seconds which is a distinct cloud feature (seen also in the AUGUST experiment.)

continued to sense less of the warm atmosphere. Then the thermal emission signal began to increase again as the scan progressively viewed warmer and warmer morning areas of the surface. To test this concept quantitatively, Paige used a delta-Eddington spherical shell model developed for the Mars Observer limb sounder. He found that a water ice haze with a scale height of 5 km (isothermal atmosphere at 200 K, surface at 175 K) could produce a thermal brightness signature matching the one in Figure 11. A similar abundance of dust particles also could produce the same result. The thermal profiles in Figure 11 and Figure 12 differ in degree of limb brightening. Either a local difference in the temperature profile between the atmosphere and the surface, or a local difference in the opacity of the atmosphere is indicated. Temperature and opacity effects cannot be separated using only one channel.

In Figure 11 and Figure 12, the visible channel recorded for the morning limb a significantly different pattern than did the thermal emission channel. The visible radiance increased for about 24 seconds before the onset of the first infrared signal. This relationship implies the presence of visible scatterers in the atmosphere to about 70 km above the physical surface, well above the region where Termoskan sensed tangible thermal emission. This result is consistent with our earlier conclusion that the visible optical depth is significantly larger than the infrared optical depth. It is interesting to note that our visible channel profiles appear very similar to those presented in Jaquin, *et al.*, 1976.

Figure 13, displays data from the evening limb crossing of scan 3. Time on the horizontal axis refers to a local data file. It is not tied into the full panorama. Here the situation is reversed from the morning limb: a peak in brightness was recorded in the visible but not in the infrared channel. Viking observations suggest transient early morning phenomena but not expected similar effects on the evening limb. Furthermore, because the surface absorbs sunlight much more efficiently than the atmosphere, it is much warmer at the end of the day. Thus surface emission overwhelms emission from atmospheric particles near the evening limb. (Note the differences in DN scale between morning and evening scans). Therefore, no limb brightening is observed in the thermal emission from the evening limb.

The extent of the visible profile for the evening limb implies at least 60 km of scattering atmosphere. Figure 14 shows a second evening limb profile also taken during panorama 3. The peak in visible brightness at 479 seconds corresponds to a distinct cloud feature. Because this cloud and the higher one on Figure 14 are so sharply defined indicates that there is not a significant scattered light problem in the optics of the instrument. This stratospheric cloud feature may cor-

relate with that observed in the AUGUST experiment, also reported in this issue.

VI. PHOBOS SHADOW MEASUREMENTS

Termoskan observed the shadow of Phobos on the surface of Mars during two of its four panoramas. For one area, shown in Figure 5, we combined the observed decrease in visible illumination of the surface with the observed decrease in brightness temperature produced by that shadow to calculate thermal inertias of the uppermost fraction of a millimeter. From this calculation we find values of thermal inertia that are significantly lower than those derived from Viking IRTM measurements (Palluconi and Kieffer, 1981; Kieffer, *et al.* 1977). The IRTM measurements are sensitive to centimeter depths.

First we consider the nature of the shadow on Mars' surface. There are seven factors that can influence its shape and intensity. First is the geometric shape of Phobos. Phobos is in synchronous rotation about Mars, was illuminated nearly end on (except near the limbs) and exhibited a nearly circular cross section of about 21 km dimension. A second effect is distortion due to projection on to the spherical surface of Mars. This effect was minor except near the limbs. Phobos' orbit is equatorial and its shadow was being projected to only 14°S latitude at the time of Termoskan's observations. Third is the distance from Phobos to where the shadow intersected Mars' surface. This distance changed only an insignificant amount over the timescale of the observation. Similarly, local topography could cause a significant distortional effect only if the shadow crossed through very major topographic relief, e.g. Valles Marineris. Fifth is the penumbral effect. The shadow of Phobos is always completely penumbral, deepest at its center, and diminishing toward the edges. Sixth, atmospheric scattering further diffuses the shadow, reducing its maximum depth while increasing its size over the purely penumbral effect. All of the above mentioned effects influence any observations of Phobos' shadow.

In our observations, there is a further effect on the apparent shape of the shadow: the relative motion of the spacecraft's field of view with respect to Phobos' shadow. Termoskan is a scanning instrument and the geometry of the observation was unusual. Phobos and the spacecraft were nearly coorbiting at the time of observation. Termoskan looked in the anti-solar direction — the same direction Phobos' shadow was projected. Therefore, Termoskan's line scanning system tended to follow the shadow on the surface, causing an apparent elongation of the shadow in the panorama. There was modulation of the apparent shadow because of a slight E-W rocking motion of the spacecraft. Figure 15 shows telemetry data taken before and after

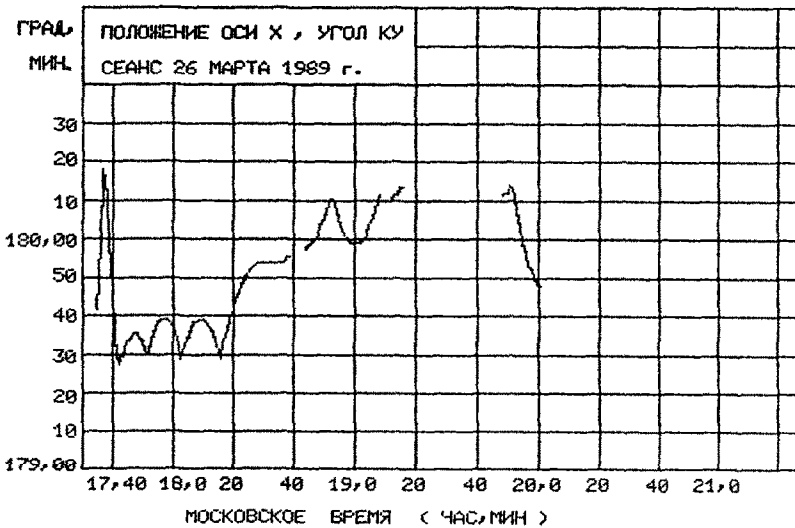
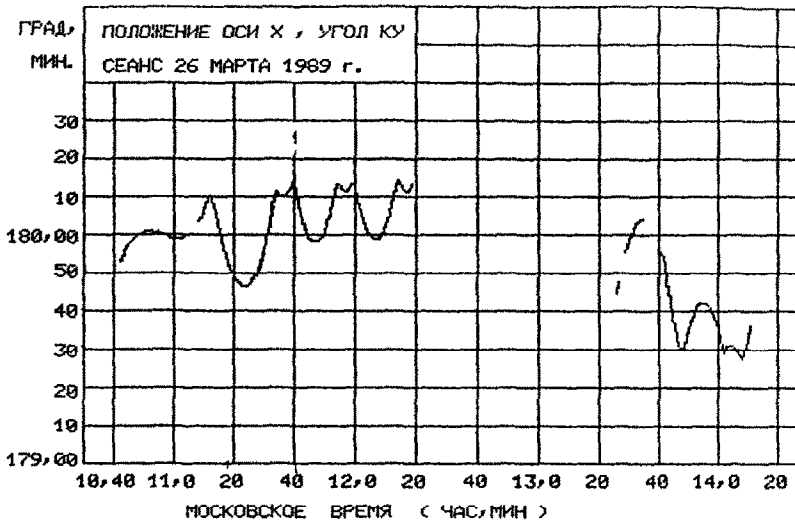


Figure 15: Deviations of the spacecraft's field of view from looking anti-solar. Horizontal axes are in Moscow Time (hour, minute). Vertical axes measure deviation from anti-solar (180 degrees) in degrees and minutes. This telemetry data was taken before and after the Termoskan panoramas. The upper graph corresponds to the time just before and just after the first March 26 panorama. Similarly, the lower graph is for the second March 26 panorama.

which depicts the magnitude of the rocking motion as function of time. In Figure 5, the field of view rocked first past the beginning of the shadow, then progressively through the shadow, and finally past the end of the shadow. Thus, an apparently elliptical shadow appears first in the visible. Subsequently there is a band of cooling in the infrared channel resulting from the shadow's passage.

We assumed the E-W rocking motion to be uniform over the brief shadow observation shown in Figure 5. We calculated that angular motion by ascribing the additional E-W shadow length (in seconds) as compared to the N-S length, which is unaffected by the rocking motion. The angular rate found is 3×10^{-5} radians/seconds, in good agreement with the spacecraft data of Figure 15. We then could connect the observed infrared cooling to the actual time since beginning of eclipse at each locality. Next we derived the input solar flux from the shadow data. Figures 16 and 17 show E-W profiles across the shadow area. Figures 18 and 19 show N-S profiles. (The close correspondence of the N-S dimension of the shadow in both the visible and infrared is an independent demonstration of the absence of significant visible light scattering in the Termoskan instrument). We determined the actual physical duration of the shadow to be about 23 seconds, from the length of a N-S profile, and the known orbital speed of Phobos, and the rotation speed of Mars. The visible brightness variation of the N-S profile is the same as the true E-W profile. Finally, we combined the inferred brightening vs. time of the shadow passage, now properly corrected for the spacecraft motion, as the input to an adaptation of the Clifford, *et al.* (1987) one dimensional, finite difference thermal model for a homogeneous surface. Figure 20 shows our results.

We find thermal inertias varying from 0.8 to 1.2 (in units of $10^{-3} \text{ cal cm}^{-2} \text{ s}^{-1/2}$) by comparing the model results with the temperature drops observed in the infrared scan. These values of thermal inertia are lower by factors of 2 to 4 than the thermal inertias derived from Viking IRTM measurements (Kieffer *et al.*, 1977) for the same area (Figure 21). Viking-derived inertias are sensitive to the upper few centimeters of the surface, whereas the Phobos eclipse shadows last only a few tens of seconds and effect only the upper tenths of a mm of the surface. Our results imply that there is a thin layer of highly insulating material, for example a thin, loosely packed dust layer, on the surface that overlies a layer of less insulating material. The depth of the surface that Termoskan sampled includes the same vertical depth that the visible albedo measurements sample. Note that the thermal inertias derived here ignore downward atmospheric infrared flux. Haberle and Jakosky, (1990), have suggested that downward atmospheric effects are much more significant than the 2% estimate used by Kieffer, *et al.*, 1977 and Palluconi and Kieffer, 1981. Adding

downward atmospheric infrared flux to our model would decrease our derived thermal inertias, thus making the thermal inertias we have presented here upper bounds and increasing the difference with Palluconi and Kieffer (1981) IRTM derived thermal inertias. We will in the future add atmospheric re-radiation contributions to our model and we will compare our results with the soon to be published Haberle and Jakosky, 1990.

At the present we have only analyzed one region. Termoskan obtained shadow observations around much of Mars at a latitude of 14 degrees South. As more data become available, we shall expand our analysis to other regions that exhibit useful Phobos shadows. More detailed modelling, when combined with greater longitudinal coverage, should give enhanced insight into the variation of the upper few hundred microns of the Mars equatorial surface over horizontal distances as small as two kilometers.

VII. CONCLUSIONS

We examined about 25% of the entire Termoskan data set quantitatively. The decalibrated infrared channel agrees to within +2 to +3 K of the processed Viking IRTM data. This difference includes not only changes in the Termoskan preflight calibration, but also residual error in the Viking data set. Furthermore, there may have been small differences in the thermal emission from Mars atmosphere and surface over the intervening decade. We found the individual pixel response of the Termoskan thermal emission data to be very high. The Termoskan thermal emission data set is an excellent representation of the actual thermal emission from Mars' equatorial regions in February and March, 1989.

We also examined the visible channel carefully, especially to determine if instrumental scattering could explain the very low contrast of the Termoskan visible panoramas. We searched for evidence of scattering by using the visible shadow from Phobos on the surface of Mars and the induced change in thermal emission, and also the limb profiles. No instrumental visible light scattering was evident in the Termoskan data. Thus, the visible data set is also of great value, especially in the limb areas where useful vertical resolution is available. We could not test the absolute photometric accuracy of the visible channel, but the data appear satisfactory for relative photometric measurements.

Limb brightening in the thermal radiation channel from the morning limb was consistently present. This is an important new result. We postulate that the limb brightening is caused by the thermal emission from dawn ice crystals in equilibrium with an atmosphere warmer than the surface. The Termoskan visible channel also defined a highly scattering atmosphere in the

East-West Profile - VIS Channel

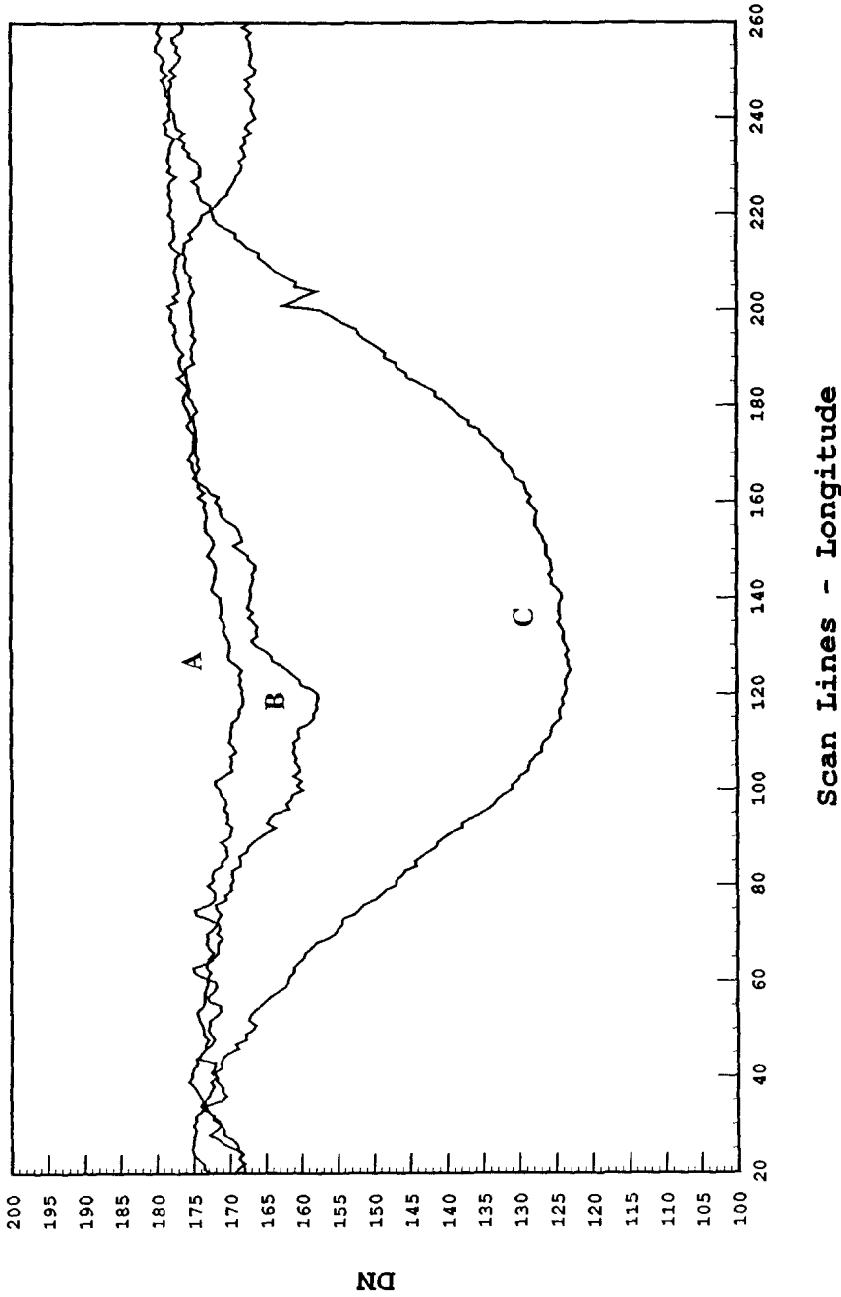


Figure 16: East-West profile - VIS channel. Reflectance from Martian surface as measured by visible channel on Termoskan. The curves in the figure are again an average of ten scan lines. The line A is retrieved from just outside (south) of shadow region (15 deg S). The line B is the same but just north of shadow (13 deg S). The line C goes straight through the middle of the shadow area (14 deg S). The plot runs from 119° W at the left to 113° W.

East-West Profile - TIR Channel

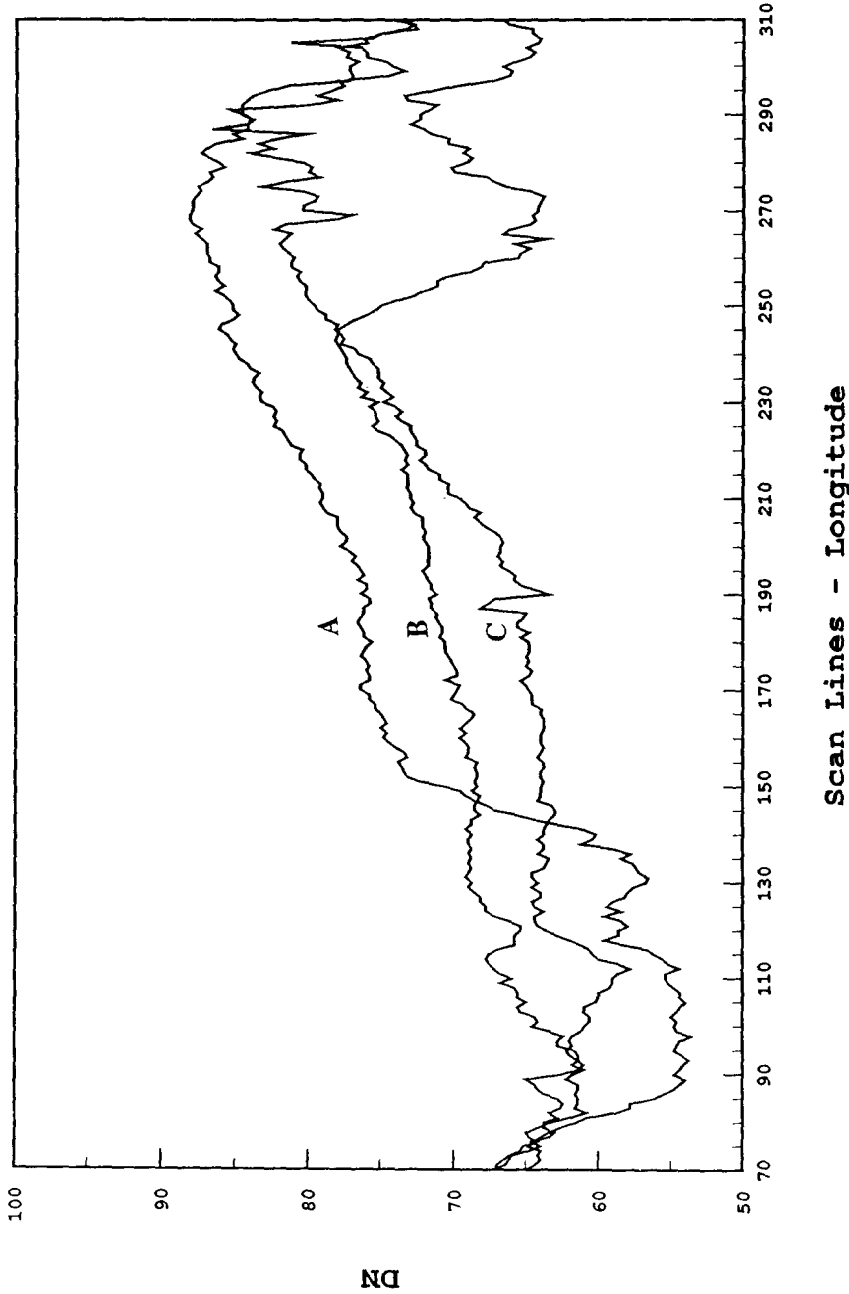


Figure 17: East-West profile - TIR channel. Thermal emission from Martian surface as measured by thermal infrared channel on Termoskan. The curves in the figure are an average of ten scan lines. The lines A, B and C are retrieved from the same region as in the previous figure. Note the general trend of increasing temperatures towards east. The plot runs from 118° W at the left to 112° W.

North-South Profile - VIS Channel

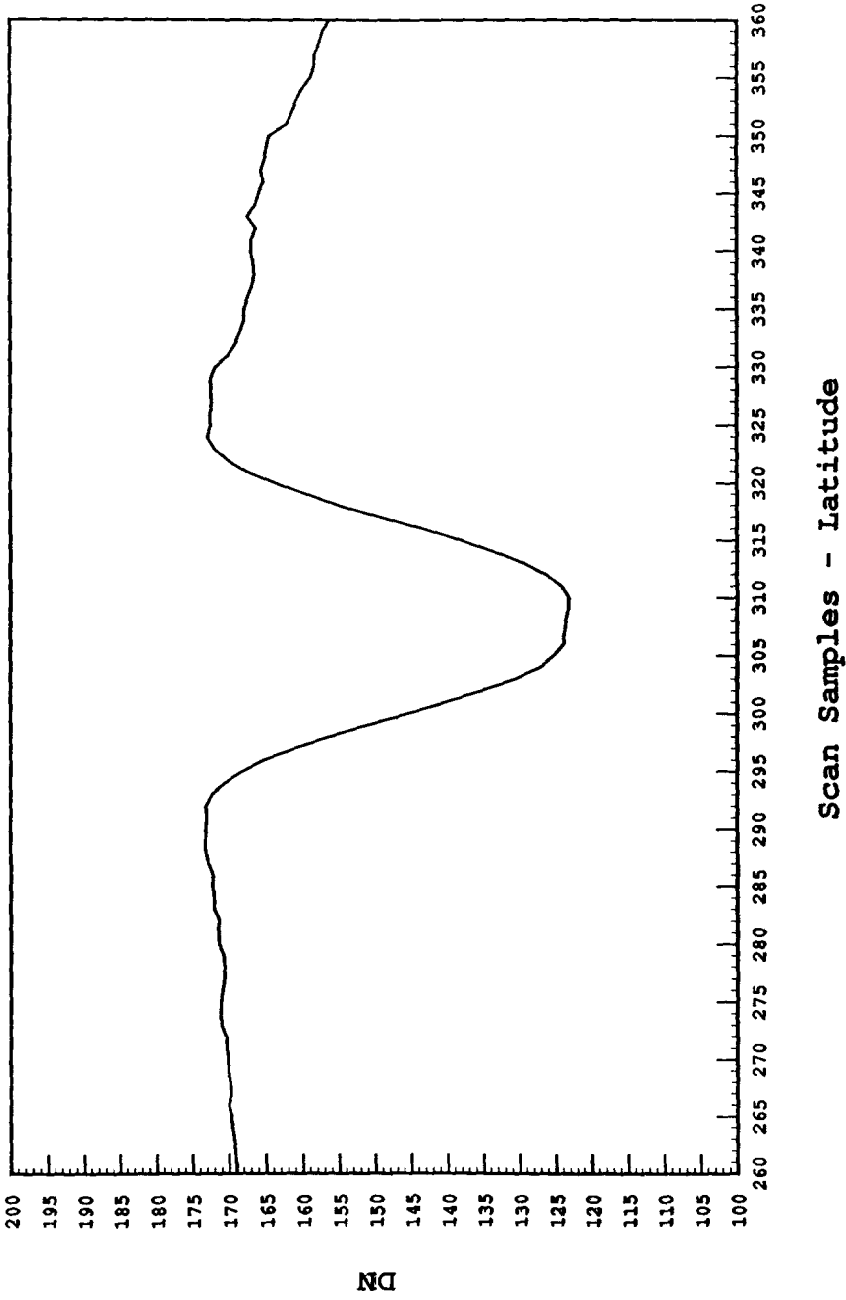
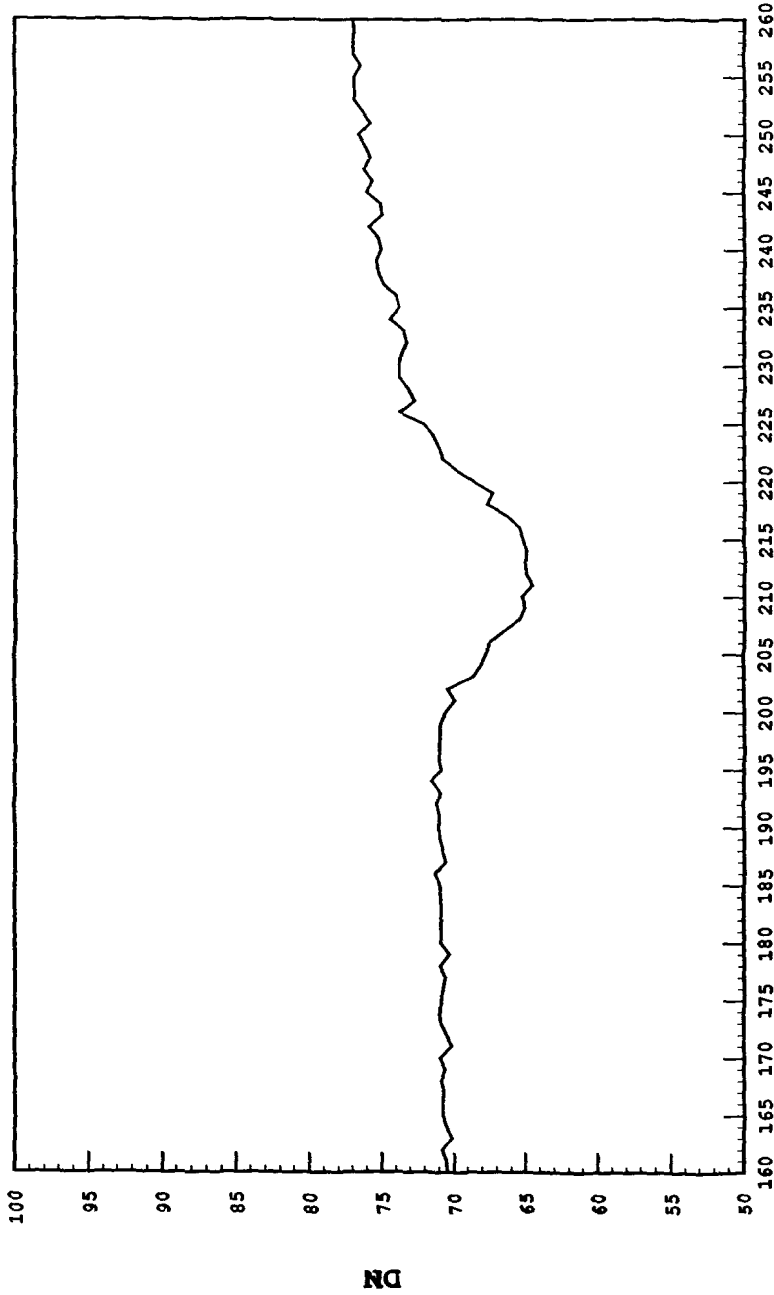


Figure 18: North-South profile - VIS channel. Reflectance from Martian surface as measured by visible channel on Termoskan. The curve plotted in the figure is an average of ten scan lines centered on the darkest part of Phobos' shadow on the surface (117 deg W, 14 S). Note the high ratio of signal vs noise. The plot runs from approximately 13.5° S at the left to 14.5° S.

North-South Profile - TIR Channel



Scan Samples - Latitude

Figure 19: North-South profile - TIR channel. Thermal emission from Martian surface as measured by thermal infrared channel on Termoskan. The curve plotted in the figure is an average of ten scan lines centered on the darkest (i.e. coldest) area of Phobos shadow on the surface (116 deg W, 14 deg S). Note the lower ratio of signal vs noise compared with the visible channel. Also note the very regular 1 DN variations every eighth pixel. The plot runs from approximately 13.5° S at the left to 14.5° S at the right.

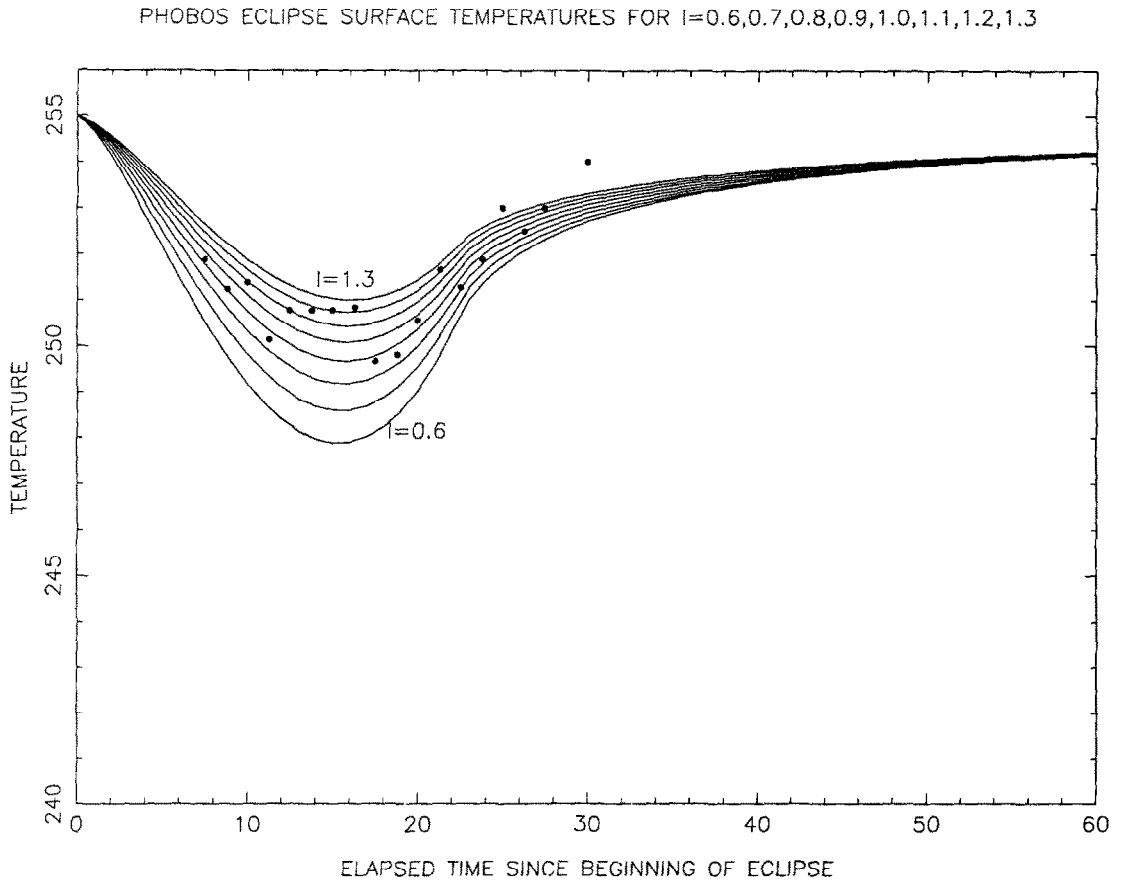


Figure 20: Phobos eclipse surface temperatures. The lines in this plot are modeled temperatures for the surface of varying thermal inertia (from 0.6 to 1.3). The dots are experimental data retrieved from the thermal infrared channel. They are derived from 10 line averages of temperature drops at the center of the shadow relative to comparable points outside the shadow. The temperature drops have been subtracted from 255 K to facilitate comparison with our model results. We chose 255 K for the plot presented here because it is a typical temperature from the shadowed region. The experimental data values fall in general between modeled curves corresponding to thermal inertias of 0.8 and 1.2.

Surface Thermal Inertia - from Viking IRTM

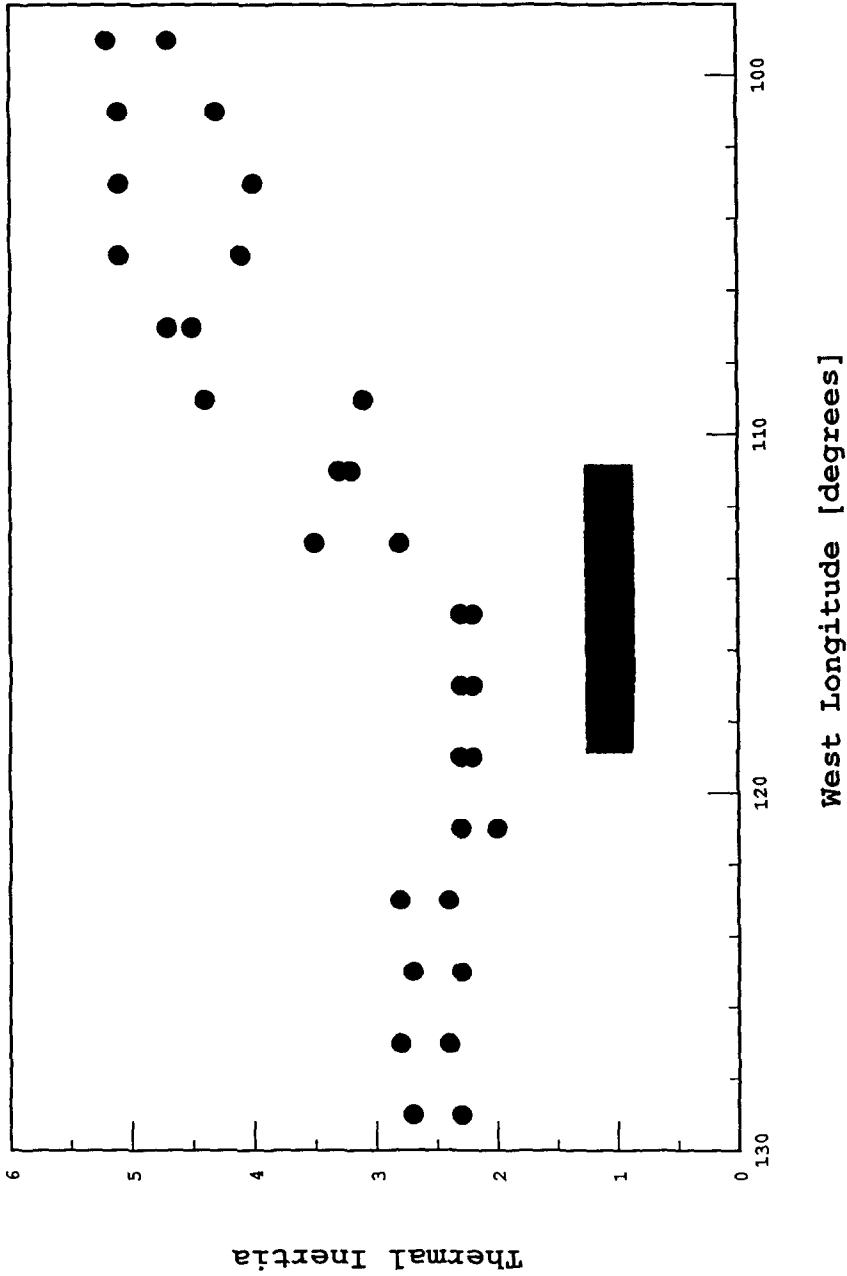


Figure 21: Surface thermal inertia from Viking IRTM. This plot shows the thermal inertia calculated for this area from Viking IRTM plotted as circles. The 2 deg by 2 deg bins of thermal inertias yield typical values of between 2.0 and 2.5 in the studied region (110-120 deg W, 13 and 15 deg S). For comparison, the approximate values derived from Phobos shadow measurements are shown as a box.

visible that appears to extend 60 to 70 kilometers above the limb. Most of this scattering atmosphere is too cold to be recorded in the infrared channel. On the evening limb the visible channel recorded that a high haze may correlate with that discovered in the AUGUST experiment. Other faint cloud features are present.

We expect comprehensive analyses of the total data set to lead to a precise location of the geometric limb, and to a high resolution description of the vertical structure of the Mars atmosphere. In addition, careful analysis of the visible signature of the eclipse shadow should help clarify the scattering properties of the Mars atmosphere. These can be compared with the Termoskan limb profiles and with the KRFM photometric scans across Mars.

The Termoskan limb visible and thermal emission profiles are of great significance to the PMIRR. The timely availability of the model calculations from the PMIRR team enabled us to recognize promptly the significance of the limb brightening in the Termoskan data.

The Termoskan observations display high resolution thermal structure associated with variations in the Martian regolith. There is geologic promise in a careful quantitative comparison between the Termoskan data and the Viking orbiter IRTM and TV images. Crumpler *et al.*, (1990) in a preliminary report state that Termoskan thermal data can help differentiate geological units on the southern flanks of Arsia Mons. Furthermore, new radar images of high resolution cover portions of the same equatorial area as Termoskan (Muhleman, *et al.*, 1990). These offer an important further data comparison. Preliminary analysis of the thermal response to one passage of the shadow of Phobos suggests that the uppermost fraction of a millimeter of Mars' surface there may be 2–4 times more insulating than indicated by IRTM, which sampled to a depth of some centimeters.

The high thermal contrast in myriad surface features seen in the limited sample of Termoskan data highlights the potential of the Mars Observer Thermal Emission Spectrometer instrument (TES). TES intends to construct a map of the entire planet at only slightly worse resolution than Termoskan (3 kilometers versus 2 kilometers). The TES map will incorporate both day and night thermal measurements and also surface spectral characteristic.

An improved Termoskan was selected to fly on the Mars '94 mission of the U.S.S.R. Current plans project two orbiters in highly elliptical, near-polar orbits, with periapsis initially in the 40 to 45 degree Northern latitude range. Termoskan 2 may achieve as high a surface resolution as 100 meters under optimum conditions. Termoskan 2 and the Mars '94 mission should complement and extend the Mars Observer PMIRR and TES measurements, and also provide independent

clues to Mars surface structure at a resolution of interest in the Mars Observer camera.

VIII. REFERENCES

- Christensen, P.R., Eolian Inter crater Deposits on Mars: Physical Properties and Global Distribution, *Icarus* 56, 1983, pp. 496–518.
- Clifford, S.M., C.J. Bartels, and E.P. Rubenstein, The Mars Thermal Model (MARSTHERM): A FORTRAN 77 Finite-Difference Program Designed for General Distribution, *Lunar and Planetary Institute*, 1987.
- Conrath, Barney. Thermal Structure of the Martian Atmosphere during the Dissipation of the Dust Storm of 1971, *Icarus*, 24, 1975, pp. 36–46.
- Crumpler, L.S., J.C. Aubele, S.L. Murchie, J.W. Head, S.T. Keddie, P.C. Fisher, J. Plutchak, A. Selivanov, M. Naraeva, Preliminary Analysis of Arsia Mons as Characterized by Phobos 2 Termoskan Instrument, Abstracts for the MEVTV Workshop on the Evolution of Magma Bodies on Mars, *Lunar and Planetary Institute*, January, 1990, p.16.
- Haberle, R.M. and B.M. Jakosky, Atmospheric Effects on the Remote Determination of Thermal Inertia on Mars, submitted to *Icarus*, 1990.
- Jakosky, B.M., The Seasonal Cycle of Water on Mars, *Space Science Reviews* 41, 1985, pp. 131–200.
- Jaquin Fred, Peter Gierasch, and Ralph Kahn. The Vertical Structure of Limb Hazes in the Martian Atmosphere, *Icarus*, 68, 1986, pp. 442–461.
- Kieffer, H.H., T.Z. Martin, A.R. Peterfreund, B.M. Jakosky, E.D. Miner, F.D. Palluconi, Thermal and Albedo Mapping of Mars during the Viking Primary Mission, *Journal of Geophysical Research* 82 (28), 1977, pp. 4249–4291.
- Martin, T.Z., A.R. Peterfreund, E.D. Miner, H.H. Kieffer, G.E. Hunt, "Thermal Infrared Properties of the Martian Atmosphere 1. Global Behavior at 7, 9, 11, and 20 μ m," *Journal of Geophysical Research*, 84(B6), 1979, pp. 2830–2842.
- Muhleman, D.O., B.J. Butler, A.W. Grossman, and M.A. Slade, Radar Spatial Imaging of Mars, In preparation for submission to *Science*, 1990.
- Paige, D., The Annual Heat Balance of the Martian Polar Caps from Viking Observations. (Ph.D. thesis manuscript, completed in February, 1985).
- Palluconi, F.D., H.H. Kieffer, Thermal Inertia Mapping of Mars from 60°S to 60°N, *Icarus*, 45, 1981, pp. 415–426.
- Pollack, J. *et al.*, Properties and Effects of Dust Particles Suspended in the Martian Atmosphere, *Journal of Geophysical Research*, 84, 1979, pp. 2929–2945.
- Sagdeev, R.Z., and A.V. Zakharov, Brief History of the Phobos Mission, *Nature*, 341, October 19, 1989, pp. 581–584.
- Selivanov, A.S., M.K. Naraeva, A.S. Panfilov, Yu.M. Gektin, V.D. Kharlamov, A.V. Romanov, D.A. Fomin, and Ya. Ya. Miroshnichenko, Thermal Imaging of the Surface of Mars, *Nature*, 341, October, 1989, pp. 593–595.
- Thorpe, T.E., "A History of Mars Atmospheric Opacity in the Southern Hemisphere During the Viking Extended Mis-

sion," *Journal of Geophysical Research*, **84**(A11), 1979, pp. 6663–6683.
Zurek, R.W., "Martian Great Dust Storms: An Update," *Icarus*, **50**, 1982, pp. 288–310.

VIV. ACKNOWLEDGEMENTS

This work was supported by NASA grant NAGW 1426.